



Integration of 3D-printed micromixers and spray drying for pulmonary delivery of antimicrobial microparticles

Brayan J. Anaya^a, Aytug Kara^a, Rafaela Raposo^b, Diego F. Tirado^c, Aikaterini Lalatsa^d, Elena González-Burgos^{e,*}, Dolores R. Serrano^{a,f,*}

^a Pharmaceutics and Food Technology Department, Faculty of Pharmacy, Universidad Complutense de Madrid, Plaza RamónSpain y Cajal s/n, 28040 Madrid, Spain

^b Sección Departamental de Fisiología, Faculty of Pharmacy, Universidad Complutense de Madrid (UCM), 28040 Madrid, Spain

^c Dirección Académica, Universidad Nacional de Colombia, Sede de La Paz, La Paz 202017, Colombia

^d CRUK Formulation Unit, Institute of Pharmacy and Biomedical Sciences, University of Strathclyde, John Arbuthnot Building, 161 Cathedral St, Glasgow G4 0RE, UK

^e Department of Pharmacology, Pharmacognosy and Botany, Faculty of Pharmacy, Universidad Complutense de Madrid (UCM), 28040 Madrid, Spain

^f Instituto Universitario de Farmacia Industrial, Faculty of Pharmacy, Universidad Complutense de Madrid 28040 Madrid, Spain

ARTICLE INFO

Keywords:

Lung infection
Microparticles
Spray drying
Azithromycin
Heparin
Microfluidics
Continuous manufacturing

ABSTRACT

Pulmonary drug delivery is crucial for treating respiratory diseases, requiring precise particle engineering for optimal therapeutic efficacy. This study demonstrates a novel integration of 3D-printed microfluidic micromixers with spray drying technology to produce inhalable azithromycin (AZM) microparticles targeting lung delivery. The formulation demonstrated effective deep lung deposition at both 30 L/min and 60 L/min flow rates. At 30 L/min, AZM-loaded microparticles achieved enhanced performance with 1.2-fold higher Fine Particle Fraction (FPF) < 5 μm and 1.4-fold higher FPF < 3 μm compared to 60 L/min. Microparticles (25 mg) can deliver an efficacious dose of AZM to the lung, exceeding the reported epidemiological cut-off for *Haemophilus influenzae* (4 mg/L) by approximately five-fold while maintaining high human bronchial epithelial cell viability (> 94 %). The antibacterial efficacy against *H. influenzae* was confirmed, demonstrating the therapeutic potential against lung pathogens. The successful deep lung deposition at both air flow rates reflects the robustness of the formulation design, making it suitable for diverse patient populations with varying inspiratory capabilities, including children and elderly patients.

1. Introduction

Pulmonary drug delivery has emerged as a valuable approach for treating lung diseases such as asthma, chronic obstructive pulmonary disease (COPD), pulmonary arterial hypertension (PAH), and select pulmonary infections. While systemic antimicrobials administered orally or intravenously remain the standard treatment for pulmonary infections, localized drug delivery to the lungs offers the advantage of directly targeting the site of action, potentially enhancing therapeutic efficacy and minimizing systemic side effects. Devices such as dry powder inhalers (DPIs), metered dose inhalers (MDIs), and nebulizers facilitate efficient drug distribution and absorption by delivering particles with aerodynamic diameters ranging from 1 μm to 5 μm, optimizing deposition in the respiratory tract. Devices such as DPIs and nebulizers

are preferred for antimicrobial delivery due to their ability to deposit higher doses into the lungs, while MDIs are primarily used for bronchodilator and corticosteroid administration (Gondhale-Karpe, 2023; Ibrahim et al., 2015; Kumar et al., 2022; de Pablo et al., 2017; Celi et al., 2023; Kuga et al., 2023).

In particular, DPIs offer several advantages, including deep lung deposition with high-dose delivery, ease of use, and minimized side effects. As breath-actuated devices, DPIs eliminate the need for coordinating inhalation with device activation, improving patient compliance. While their lower carbon footprint and cost-effectiveness are important environmental and economic benefits, compliance is primarily driven by their user-friendly design and consistent therapeutic outcomes compared to MDIs and nebulizers (Knap et al., 2023; Chandel et al., 2019; Ossebaard et al., 2021). Traditionally, DPIs require inspiratory

* Corresponding authors at: Pharmaceutics and Food Technology Department, Faculty of Pharmacy, Universidad Complutense de Madrid, Plaza RamónSpain y Cajal s/n, 28040 Madrid, Spain (D.R. Serrano). Pharmacology, Pharmacognosy and Botany, Faculty of Pharmacy, Universidad Complutense de Madrid (UCM), 28040 Madrid, Spain (E. González-Burgos).

E-mail addresses: elenagon@ucm.es (E. González-Burgos), drserran@ucm.es (D.R. Serrano).

<https://doi.org/10.1016/j.ijpharm.2025.125493>

Received 28 November 2024; Received in revised form 14 March 2025; Accepted 15 March 2025

Available online 17 March 2025

0378-5173/© 2025 The Authors. Published by Elsevier B.V. This is an open access article under the CC BY license (<http://creativecommons.org/licenses/by/4.0/>).

flow rates of 60 L/min for optimal drug particle deposition in the lungs, which can be challenging for patients with reduced respiratory capacity, such as those with severe COPD or asthma. By optimizing the aerodynamic particle size, DPIs can be designed to achieve effective deep lung deposition at lower flow rates (30 L/min or even lower), similar to MDIs and nebulizers (Liu et al., 2023; Rahman et al., 2022; de Pablo et al., 2023).

The significant impact of COVID-19 on respiratory function, particularly in patients with pre-existing conditions such as bacterial infections, underscores the urgent need for innovative therapeutic strategies to address the unique challenges faced by these individuals (Orea-Tejeda et al., 2023; Ribeiro Baptista et al., 2022; Kjellberg et al., 2024). The optimization of DPIs to achieve effective deep lung deposition at lower inspiratory flow rates offers a promising approach for patients with reduced respiratory capacity due to COVID-19 or other underlying conditions. By designing DPIs with optimized aerodynamic particle sizes, these devices can deliver high doses to the lungs while minimizing side effects. Developing DPIs specifically tailored to the needs of COVID-19 survivors and those with compromised lung function could significantly enhance therapeutic outcomes and quality of life, highlighting the importance of ongoing research and innovation in this field.

3D printing technologies have emerged as a transformative tool in pharmaceutical applications, providing innovative solutions for treating lung diseases. This cutting-edge technology enables the development of highly customized and patient-specific medical devices, drug delivery systems, and complex tissue models, essential for addressing the unique challenges associated with pulmonary conditions (Tyagi et al., 2024; Haque et al., 2018; Serrano, et al., 2023; Anaya et al., 2023; Kara et al., 2023; Yuste et al., 2023). The capability of 3D printing to produce intricate geometries and complex compositions with high precision makes it particularly well-suited for creating devices used in lung drug delivery.

3D-printed microfluidic micromixers offer a compact and versatile platform for the synthesis of particles ranging from nanometers to micrometers in size. These micromixers integrate multiple unit operations, including processing, separation, reaction, and detection, enabling rapid and efficient analysis of the synthesized particles. The incorporation of microreactors and micromixers is essential for producing particles with uniform size distribution and enhanced encapsulation efficiency. Precise control over particle size and distribution is achieved by manipulating flow rates, solvents, surfactants, and polymer compositions within simple and adaptable designs. This level of control is crucial for applications such as drug delivery systems, where particle characteristics significantly influence the efficacy and biodistribution of the encapsulated therapeutic agent (Wu et al., 2022; Osouli-Bostanabad et al., 2022; Puglia et al., 2005; Kara et al., 2021; Patil et al., 2023).

The AZM-heparin inhalable co-formulation presents a novel approach to treating complex respiratory infections, including COVID-19. AZM exhibits potent anti-inflammatory effects in chronic respiratory diseases, significantly reducing exacerbations in COPD and cystic fibrosis (Segal et al., 2017; Oliver and Hinks, 2021). AZM modulates the lung microbiota, enhancing anti-inflammatory metabolites and mitigating pro-inflammatory responses in *Pseudomonas aeruginosa* infections (Leal et al., 2016). Crucially, AZM inhibits inflammasome activation, a key pathway in innate immune responses, by reducing the secretion of IL-1 and other pro-inflammatory cytokines (Gualdoni et al., 2015). This mechanism is particularly beneficial in respiratory diseases where excessive inflammasome activation contributes to pathology. This multifaceted action, targeting host immunity, pathogen virulence, and inflammatory cascades, positions AZM as a key therapeutic agent for complex respiratory conditions characterized by chronic inflammation and recurrent infections (Saris et al., 2022; Joelsson et al., 2020; Patel, et al., 2018). Conversely, heparin exhibits dual efficacy in COVID-19 treatment. Its well-established anticoagulant properties reduce thromboembolic risks associated with virus-induced endothelial damage,

while its potential antiviral effects may inhibit SARS-CoV-2 cellular entry and replication (Mangiafico et al., 2022; Costanzo et al., 2020; Tree et al., 2021; Zang et al., 2022). This multifaceted action positions heparin as a critical therapeutic agent in managing the complex pathophysiology of COVID-19, particularly for high-risk, critically ill patients. We have previously demonstrated the synergistic combined effect between heparin and AZM against lung pathogens (Anaya et al., 2024).

The hypothesis underlying this work is that 3D-printed microfluidic micromixers could be useful to tailor the particle size of DPI formulations enabling a continuous manufacture methodology to enhance both yield and efficiency of the process. Microfluidic devices allow for an effective mixing of drugs and excipients within their microchannels. The selection of suitable solvents will guarantee controlled precipitation targeting the ideal particle size for lung delivery. The integration of microfluidic micromixers with spray drying could tune the final particle characteristics for an excellent particle lung deposition (Kara et al., 2021; Ongoren et al., 2024; Kara et al., 2023; Lechanteur and Evrard, 2020). Spray drying is a scalable technology widely used by pharmaceutical industries for the manufacture of dry powders (Gholizadeh-Hashjin et al., 2024; Malamatarı et al., 2020; Al-Zoubi et al., 2021; Baumann et al., 2021). We have previously demonstrated the feasibility of preparing AZM-loaded microparticles using spray drying (Anaya et al., 2024). In this work, we will go beyond the state-of-the-art to demonstrate the integration of a continuous manufacturing platform consisting of a microfluidic micromixer coupled with spray drying. This combination of both technologies is capable of controlling particle precipitation with an optimal particle size towards antibacterial inhalable microparticles targeting deep lung regions being less dependent on the patient's inspiratory flow rate, thereby reducing interpatient variability and making the devices suitable for a broader range of patients, including young children and the elderly. The mixing process of AMZ-loaded microparticles was modelled using computational fluid dynamics. Microparticles were fully characterised and *in vitro* lung deposition was assessed. The biological activity was tested against mammalian cells and bacteria.

2. Material and methods

2.1. Materials

Heparin sodium salt (purity > 95 %), CAS # 9041-08-1 from porcine intestinal mucosa, Lot No. A0411030 (203.5 IU/mg, Acros organics) was purchased from Fisher Scientific (Madrid, Spain). Azithromycin (AZM) with purity \geq 95 % was bought from Kemprotec (Cumbria, UK) while leucine with purity \geq 98 % was purchased from Sigma Aldrich (Madrid, Spain). UV polymerizable commercial clear resin (405 nm) was obtained from Anycubic® (Shenzhen, China). Methanol (HPLC grade, purity: \geq 99.9 %) was purchased from Symta SL (Madrid, Spain). Anycubic Photon Mono X (LCD-based SLA printer, 405 nm light source, 0.05 mm 3840 × 2400 XY resolution, 0.01 mm Z resolution, 192 mm × 120 mm × 245 mm build volume) was purchased from Anycubic® (Shenzhen, China). HPLC-grade solvents were used. All other chemicals were of reagent grade and were used without further purification.

2.2. Methods

2.2.1. Design and 3D printing of the microfluidic device

A T-shaped toroidal micromixer was designed using Tinkercad (Autodesk®, Mill Valley, CA, USA) with 3.7 cm in length, 4.7 cm in width, and 0.6 cm in height. The device featured two separated inlet channels for the entrance of the organic and aqueous phases. Each channel was 23 mm in length and 1 mm in diameter, extending up to the junction of the inlets. Following the T junction, mixing was fostered by four interconnected 5 mm diameter circular rings of 1 mm internal channel diameter connected to the outlet. The rings were aligned with a 45°. The final microfluidic chip design was exported into a standard

tessellation language (.stl) digital file. This file was imported into Anycubic Photon Slicer Software (Anycubic®, Shenzhen, China). The (.stl) file was sliced to g-code format (.pwm) for stereolithographic (SLA) printing.

The Anycubic® Photon Mono X SLA printer was used to print microfluidic devices under photopolymerization of the Anycubic® UV sensitive transparent green resin at 405 nm. The solidified resin was adhered initially to the metal platform, and the other layers adhered to this first layer, thus creating the desired object. Each layer was 0.05 mm thick. The first eight layers were exposed to UV light longer than the others (60 s) to ensure good attachment to the metallic platform. Subsequent layers received shorter UV exposure (2 s). At the end of each layer, the UV light was turned off for 1 s, preventing unwanted parts from solidifying (Ongoren et al., 2024).

Once the microfluidic chip was printed, it was washed and cured using the Anycubic Wash & Cure Machine 2.0 (Anycubic®, Shenzhen, China). During the washing step, the microfluidic chip was immersed in isopropyl alcohol 70 % for 15 min. Subsequently, the chip was removed from the isopropyl alcohol, and channels were flushed with 5 mL of ethanol. Afterward, channels were flushed with 5 mL of water to ensure complete unpolymerized resin removal. After the washing cycle, the chip was placed in the Anycubic Wash & Cure Machine 2.0 (Anycubic®, Shenzhen, China) post-curing box for two hours under 405 nm UV light. After printing, washing, and curing, the geometry of the chip was visualized with a Xiaomi X3 pro phone with a 48-megapixel camera ($f/1.79$, $1.6\text{-}\mu\text{m}$) (Xiaomi Inc, Beijing, China).

2.2.2. Rational selection of organic solvent

Ethanol was selected as a suitable solvent for controlling particle precipitation due to its moderate polarity with a dielectric constant of 24.55 and complete miscibility with water in all proportions under normal conditions, allowing a rapid and controlled antisolvent precipitation of heparin dissolved in water. Ethanol's low boiling point ($\sim 78\text{ }^\circ\text{C}$) is advantageous for subsequent spray drying, as it readily evaporates, minimizing residual solvent in the final product. Additionally, ethanol's relatively low toxicity and environmental impact make it a safer choice compared to other organic solvents commonly used such as dimethyl sulfoxide (DMSO) (ICH, E., Impurities: Guidelines for residual solvents Q3C (R5), 2011, ICH Geneva, Switzerland), aligning with green chemistry principles (Welton, 2015). Its ability to induce supersaturation is crucial for maintaining the integrity of macromolecules such as heparin in the formulation.

2.2.3. Preparation and characterization of the microparticulate formulation

The aqueous phase consisted of a 50 mL solution with heparin, AZM, and leucine (75:5:20, w:w) dissolved in deionized water (10 % w/v) which was loaded into a 50 mL syringe (Fisher Scientific, Madrid, Spain). The composition was optimized based on a previous study (Anaya et al., 2024). The organic phase consisted of 50 mL of ethanol loaded in a 50 mL syringe (Fisher Scientific, Madrid, Spain). Both syringes were connected to two syringe pumps (New Era Pump Systems, NY, USA). Each syringe was fitted with a 14-gauge olive colour needle (with an outer \varnothing of 1.83 mm and inner \varnothing of 1.75 mm) (Fisher Scientific, Madrid, Spain). One end of the silicone tube (inner \varnothing 1.83 mm) was connected to the syringe needle outlet and the other end was connected to the toroidal T-mixer's inlet cylinder tied with a cable tie to avoid leakages.

A single batch was performed using a total flow rate of 10 mL/min and a 1:1 (v:v) flow ratio between the aqueous and organic phases. At 14 mL intervals, a 1 mL sample was collected from the outlet channel and subsequently analyzed using a Zetasizer (Malvern Instruments, Malvern, UK) to evaluate mixing behaviour and assess its impact on particle size (nm), and polydispersity index (PDI) (see Fig. 3).

After controlled precipitation in the microfluidic mixer, the suspension containing 5 % (w/v) solids was fed into the spray-dryer (Buchi

B191 Mini Spray Dryer, Büchi Labortechnik AG, Switzerland) equipped with a high-efficiency cyclone in the open mode. The process parameters were set as follows: $90\text{ }^\circ\text{C}$ inlet temperature, 2.5 mL/min (equivalent to 5 %) solution feed rate, 800 NL/h airflow rate, and 95 % aspirator force (equivalent to $28\text{ m}^3/\text{h}$). Under these conditions, an outlet temperature of $56\text{ }^\circ\text{C} \pm 1\text{ }^\circ\text{C}$ was recorded. Once the solution was spray-dried, the particles were collected inside the collection vessel and the following three responses were evaluated: yield, AZM-loading efficiency, and encapsulation efficiency. The yield was calculated by considering the difference in weight between the dry powder collected after the spray drying process and the total weight of solutes (excipients and AZM) introduced into the feed solution, using the following Equation (1).

$$\text{Yield (\%)} = \frac{\text{Weight of collected spray dried formulation}}{\text{Weight of solutes in the feed solution}} \times 100\% \quad (1)$$

High-performance liquid chromatography (HPLC) analysis was conducted using a Varian Prostar 230 Solvent Delivery Module, a Varian Prostar 410 Autosampler, and a Varian Prostar 310 UV-visible Detector (Varian®, Palo Alto, CA, USA). Data collection and processing were performed using the Galaxie Chromatography Data System (Varian®, CA, USA). AZM was separated on a Thermo Scientific BDS Hypersil C18 reverse-phase column ($250\text{ mm} \times 4.6\text{ mm}$, $5\text{ }\mu\text{m}$). AZM was quantified using a previously validated HPLC method by Al-Hakkani et al (Al-Hakkani, 2019). The mobile phase consisted of phosphate buffer (0.2 M KH_2PO_4 , pH 8): methanol (1:10 v/v) which was filtered through a hydrophilic $0.45\text{ }\mu\text{m}$ filter (Millipore, Millex-LCR, Merck, Madrid, Spain), and pumped at a flow rate of 1.2 mL/min. The sample injection volume was 50 μL . The column temperature was maintained at room temperature, and the detector was set at 210 nm.

For drug loading (DL) and encapsulation efficiency (EE) quantification, approximately 5 mg of powder formulation ($n = 3$) was weighed and dispersed in 1 mL of the mobile phase. The sample was then sonicated and vortexed for 5 min before centrifugation for 5 min at 5,000 rpm. The supernatant was subsequently analyzed by HPLC. AZM concentrations were determined by integrating the peak area at 15 min using a calibration curve. The linear calibration curve range was obtained over the range of 10 $\mu\text{g}/\text{mL}$ to 400 $\mu\text{g}/\text{mL}$ for unprocessed AZM, with an R^2 value of 0.9972 ($y = 0.0918x - 2.1117$). DL was calculated using Equation (2) and EE using Equation (3), both expressed as a percentage:

$$\text{DL (\%)} = \frac{\text{Weight of active ingredient}}{\text{Weight of powder formulation}} \times 100\% \quad (2)$$

$$\text{EE (\%)} = \frac{\text{Total drug encapsulated}}{\text{Total drug content}} \times 100 \quad (3)$$

Numerical simulations

Computational fluid dynamics (CFD) simulations were performed using COMSOL Multiphysics 5.6 (Burlington, MA, USA), with laminar flow and diluted species interface transport. The microfluidic chip used in the experiments was consistently designed using software to ensure that the experimental results closely matched the simulations. In addition, the flow rates were carefully matched to the experimental setup to maintain the accuracy of the comparisons (Ongoren et al., 2024).

The conservation of momentum and mass in the microfluidic chips, characterized by single-phase, incompressible, and time-dependent laminar flow, was analyzed. This analysis used the Navier-Stokes equations for momentum (Equation (4)) and the continuity equation (Equation (5)) for mass conservation (Javaid et al., 2017). The equations are expressed as follows:

$$\rho \left(\frac{\partial \mathbf{u}}{\partial t} + (\mathbf{u} \cdot \nabla) \mathbf{u} \right) = -\nabla p + \mu \nabla^2 \mathbf{u} \quad (4)$$

where (ρ) is the fluid density (kg/m^3), (\mathbf{u}) is the fluid velocity vector (m/s), (t) is time (s), (p) is pressure (Pa), and (μ) is the dynamic viscosity (Pa).

s).

$$\nabla \cdot \mathbf{u} = 0 \quad (5)$$

The equation implies that the fluid is incompressible (Chen and Shen, 2017; Ta et al., 2015). Solving these equations provided insight into the velocity and pressure fields within the system. The resulting velocity field was then used to determine the species concentration field, which was calculated using the convection–diffusion equation, expressed as (Equation (6)):

$$\frac{\partial c_i}{\partial t} + \nabla \cdot (-D_i \nabla c_i + \mathbf{u} c_i) = R \quad (6)$$

where c_i is the concentration of species (i), D_i is the diffusion coefficient ($1.2 \times 10^{-9} \text{ m}^2/\text{s}$ for water–ethanol mixture), and \mathbf{u} is the fluid velocity vector. R is the reaction rate, which was assumed to be zero. The initial concentrations of the aqueous (C_{aqueous}), and organic (C_{organic}), phases were set to $1 \text{ mol}/\text{m}^3$. These standardized concentrations were applied at their respective inlets to bind the concentration fields accurately for the dilute species transport analysis.

The density of water (ρ_{water}) was $997 \text{ kg}/\text{m}^3$; the density of ethanol (ρ_{ethanol}) was $789 \text{ kg}/\text{m}^3$; the viscosity of water (μ_{water}) was 0.001 Pa s and the viscosity of ethanol (μ_{ethanol}) was 0.0012 Pa s (Technology, 2023).

Analyzing homogeneity at the outlet of the microfluidic chip is one method used to assess mixing. The statistical measure of uniformity in the mixed solutions was determined by calculating the standard deviation of the concentration. Previous studies (Chen and Shen, 2017; Ta et al., 2015; Javaid et al., 2018) have used methods based on the standard deviation of concentration to assess the mixing in microfluidic chips. In this study, the efficacy (M) was calculated using a formula derived from the standard deviation of concentration, which is expressed as follows (Equation (7)):

$$M = 1 - \frac{\sigma}{\sigma_{\text{Max}}} \quad (7)$$

where, σ represents the standard deviation of species concentration at a given cross-section, while σ_{Max} indicates the standard deviation in a completely unmixed state. The efficacy, indicated as ' M ', is quantified on a scale where 0 corresponds to the unmixed state and 1 to a fully mixed state. The standard deviation was calculated as follows (Equation (8)):

$$\sigma = \sqrt{\frac{1}{N} \sum_{i=1}^N (c_i - c_m)^2} \quad (8)$$

where N is the number of sampling points, c_i is the mixing fraction at point (i), c_m is the optimal mixing fraction.

Morphology and particle size characterization

The mean particle size after dispersion in aqueous media ($5 \text{ mg}/\text{mL}$), polydispersity, and zeta potential were measured using a Zetasizer (Malvern Instruments, Malvern, UK). This concentration was optimized in previous studies (Anaya et al., 2025). Measurements of mean particle size and polydispersity were performed at a scattering angle of 90° and a temperature of 25°C . Before measurements, polystyrene standards (diameter = 100 nm) were measured; size results were in accordance with the nominal size of the standard particles (Serrano et al., 2015).

Transmission Electron Microscope (TEM) (JEM 1400 plus JEOL, Japan) equipped with an acceleration voltage ranging from 40 kV to 120 kV was used for imaging. A drop of an aqueous sample dispersion ($5 \text{ mg}/\text{mL}$) was placed onto a Formvar/carbon-coated grid, and the excess sample was blotted off with the Whatman $\text{N}^\circ 1$ filter paper. The samples were then negatively stained with $1\% \text{ w/v}$ phosphotungstic acid solution. Images were captured using an AMT digital camera (Smith et al., 2018).

2.2.4. Solid state characterization

Morphology

The morphology of the optimized microparticulate formulations after spray drying was characterized by Scanning Electron Microscopy (SEM) (JSM 6335F JEOL, Japan) equipped with a secondary electron detector at 15 kV . Samples were sputter coated with pure gold using a metallizer (Q150RS Metalizador QUORUM, Quorum Technologies Ltd., Lewes, UK) for 180 s under vacuum. Particle sizes were measured using ImageJ software version 1.53 t (National Institutes of Health, USA).

Powder X-ray diffraction (pXRD)

Powder X-ray analysis was conducted using a Philips®X'Pert-MPD X-ray diffractometer (Malvern Panalytical®; Almelo, The Netherlands) equipped with Ni-filtered Cu K radiation (1.54). The study was performed at 40 kV voltage and 40 mA . pXRD patterns were recorded at a step scan rate of $0.05^\circ/\text{s}$, ranging from 5° to 40° on the 2-theta scale ($n = 3$). For comparison purposes, physical mixtures of raw powder materials between API and excipients, prepared in an agate mortar and pestle were used (Anaya et al., 2023).

Fourier-Transform Infrared (FTIR) Spectroscopy

FTIR analysis was performed using a Nicolet Nexus 670–870 (ThermoFisher, Madrid, Spain). A wavelength range between 400 cm^{-1} – 4000 cm^{-1} was used with a 1 nm step scan. Spectra were interpreted using Spectragryph (version 1.2.9, Oberstdorf, Germany) software, and data normalization was carried out.

Differential Scanning Calorimetry (DSC) coupled with Thermogravimetric Analysis (TGA)

DSC-TGA standard scans were conducted using $5\text{--}6 \text{ mg}$ weight powder with nitrogen as the purge gas on an SDT Q600 instrument (TA instruments, Elstree, UK) calorimeter. A scanning rate of $10^\circ \text{C}/\text{min}$ was used from 25°C to 350°C . The instrument was calibrated using indium as the standard. The glass transition temperatures reported are the midpoint of the transition ($n = 3$) (Santamaría et al., 2024).

2.2.5. In vitro haemolysis assay

Haemolysis studies were performed with red blood cells (RBCs) to assess the toxicity of the formulation. Cells were obtained from the blood of a healthy 28-year-old male volunteer, following ethical procedures approved by Universidad Complutense de Madrid (Madrid, Spain) in EDTA coated Vacutainers® (K2-EDTA, BD Vacutainer® tubes, Becton Dickinson and Co., New Jersey, USA). The blood was centrifuged at $3,000 \text{ rpm}$ for 5 min , and hematocrit, and plasma levels were marked on the tube. The supernatant (plasma) was removed, and the erythrocytes were washed three times with an equivalent volume of $0.9\% \text{ NaCl}$ (150 mM), followed by centrifugation at $3,000 \text{ rpm}$ for 5 min at each step. After washing, the supernatant was discarded, and the RBCs were resuspended in PBS pH 7.4 to a final concentration of $4\% \text{ w/w}$. Subsequently, a volume of $180 \mu\text{L}$ was added to each well (Pineros et al., 2017). Samples (microparticles, excipients, and APIs) were dispersed with PBS (1X, pH 7.4) to produce 8 serial dilutions of AZM concentration ranging from $200 \mu\text{g}/\text{mL}$ to $1.65 \mu\text{g}/\text{mL}$ ($20 \mu\text{L}$, $n = 3$). Triton® X-100 (Sigma-Aldrich CO, St. Louis, USA) in PBS (1X, pH 7.4) prepared at $20\% \text{ w/v}$ or PBS (1X, pH 7.4) were used as a positive and negative control ($20 \mu\text{L}$) respectively. The plates were then incubated at 37°C for 1 h (Mommert GmbH + Co., Schwabach, Germany). Subsequently, the plates were centrifuged at $1,500 \text{ rpm}$ for 5 min to pellet intact erythrocytes. The supernatant ($100 \mu\text{L}$) was transferred to a clear flat-bottomed 96-well plate. Absorbance (ABS) was measured at 570 nm using a plate reader (BioTeK, Ekx808). The percentage of haemolysis was calculated using the Equation (9):

$$\% \text{Haemolysis} = \frac{\text{ABS1} - \text{ABS2}}{\text{ABS3} - \text{ABS2}} \times 100 \quad (9)$$

where ABS1 sample represents the absorbance of the sample, ABS2 is the absorbance of the negative control, and ABS3 is the absorbance of the positive control. The concentration needed to produce $50\% \text{ haemolysis}$

(HC₅₀) was calculated using Compusyn™ v1.0 (Composyn Inc., New Jersey, USA).

2.2.6. Antibacterial *in vitro* disk diffusion assay

The antibacterial effect of the loaded microparticles was tested against *Haemophilus influenzae* (CECT 8452). The antimicrobial activity was tested by Diagnostic Sensitivity Test (DST) with a chocolate horse blood agar plate (Oxoid™, Thermo Scientific, Madrid, Spain). AZM-loaded microparticles dispersed in deionized water (23 mg/mL equivalent to 0.75 mg/mL of AZM) were loaded (20 µL) onto 6 mm in diameter paper disks and placed in the center of agar plates (corresponding to a final AZM dose of 15 µg onto each paper disk). Commercial disks of AZM (15 µg, Oxoid™, Thermo Scientific, Basingstoke, UK) were used as a control. Inhibition zone diameters were measured with a caliper (Cole Parmer, Fisher Scientific, Madrid, Spain) at points where there was complete inhibition of bacterial growth after 24 h of incubation. Isolates were classified as AZM susceptible (S) when the zone of inhibition was greater than ≥ 12 mm according to the National Committee for Clinical Laboratory Standards (NCCLS) (Jones et al., 1994).

2.2.7. *In vitro* lung deposition

A Next Generation Impactor (NGI; MSP Corporation, Shoreview, USA), connected to an HCP5 vacuum pump (Copley Scientific, Nottingham, UK) through a critical flow controller (TPK 2000 Copley Scientific, Nottingham, UK) was used. The NGI apparatus comprised seven stainless compartments (stages), a stainless-steel induction port, and one micro-orifice collector (MOC). To ensure accurate analysis and prevent particle bouncing, the cups of the impactor were coated with a solution of 2 % (w/v) Tween 20 in ethanol and led the solvent to evaporate before use. Airflow of 30 L/min and 60 L/min was set using a TSI 4,000 series Mass Flow Meter 4040 (TSI Incorporated, Shoreview, USA), with an inhalation time of 8 s and 4 s and a total inhaled air volume of 4 L. For the aerosolization, a hydroxypropyl methylcellulose capsule (No. 3) filled with 25 mg ± 1 mg of formulation (*n* = 3) was placed in a Handihaler (Boehringer, Ingelheim am Rhein, Germany) device. The formulations deposited in each part of the NGI were quantified using the previously described HPLC method. The mass median aerodynamic diameter (MMAD) and fine particle fraction (FPF) (<3 µm and < 5 µm) were calculated to evaluate the *in vitro* deposition of the tested formulations. MMAD was calculated by plotting cumulative particle mass percentage versus aerodynamic diameter on log-probability paper using all NGI stages. FPF values were expressed as a fraction of the emitted dose, calculated based on the AZM mass deposited on impactor stages relative to the total emitted dose (Anaya et al., 2025). Stage cut-off diameters were determined according to Marple et al. (2003) (Marple et al., 2003).

2.2.8. *In vitro* cell culture assays

Cell culture conditions

Human bronchial epithelial Calu-3 cells, obtained from ATCC (No. HTB-55, Lot. 61449062), were cultured in DMEM/F-12 with glutamine supplemented with 10 % Fetal Bovine Serum (FBS) and 1 % penicillin/streptomycin. Murine macrophage J774A.1 cells (ATCC® TIB-67™) were cultured in RPMI-1640 medium supplemented with 10 % FBS and 1 % penicillin/streptomycin. The cells were maintained at 37 °C in a humidified incubator with 5 % CO₂.

Cell viability assay

MTT assay was used to assess cell viability. Cells were seeded in 96-well culture plates at a density of 3.0 × 10⁴ cells per well (Calu-3 cells) and 1.0 × 10⁴ cells per well (J774A.1 cells).

Cells were treated with different concentrations of AZM ranging from 0.10 µg/mL to 50 µg/mL for 24 h. Triton-X solution (5 %) was used as a positive cytotoxic control. MTT solution (5 mg/mL) was added (100 µL), and cells were incubated for 4 h in the darkness. Formed formazan crystals were then dissolved in isopropyl alcohol (Calu-3 cells) or DMSO (J774A.1 cells). Absorbance was measured at 550 nm using a

Spectrostar BMG microplate reader (BMG LABTECH, Ortenberg, Germany). The percentage of viable cells was calculated using untreated cells as control, being considered as 100 % cell viability. MTT assays were done in triplicate.

2.2.9. Statistical analysis

Statistical analysis was performed via a one-way ANOVA test using Minitab v.19 (Minitab Ltd., Coventry, UK) followed by Tukey's test (95 % level of significance). The results were plotted using Origin 2021 (OriginLab Corporation, Northampton, MA, USA).

3. Results

3.1. Microfluidic device characterization

Fig. 1A-B displays the computer-aided design (CAD) of the 3D printed microfluidic device fabricated using SLA technology, along with the final prototype, showcasing the successfully printed model and detailing the dimensions of the internal channels. The dimensions of the 3D-printed device matched closely with those in the design. Channels were opened after appropriate flushing with ethanol and water.

Fig. 2 illustrates the changes in velocity, pressure, and aqueous phase concentrations during mixing within the microfluidic chip simulations using COMSOL. The velocity reached up to 0.3 m/s, with the fluids primarily interacting at the intersections of the circular sections. The pressure gradually decreased towards the outlet, indicating that most of the mixing occurred at these intersections, with only a small portion extending into the circular regions. The concentration field of the aqueous phase, where the API is located, demonstrates that despite a higher concentration at the intersections, the overall mixing within the microfluidic device was homogeneous and nearly fully mixed. This can be seen in Fig. 2C, where the outlet concentration is closer to 0.5 – indicating a balanced mixture – compared to 1, which would indicate only the aqueous phase, and 0, which would indicate only the organic phase.

This result aligns with the calculated mixing index (*M*) of approximately 0.943, where a value of 1 indicates a fully mixed state and 0 indicates no mixing. These results indicate a high level of mixing efficiency within the microfluidic chip, supporting the effectiveness of the design used in this study.

The microfluidic mixing process enables the consistent production of nanoprecipitates with controlled size distributions (Fig. 3, Table S1). Particle size was measured at different time points throughout a 100 mL mixing cycle, with an average size of 170 nm. Across most time points, particle sizes remained within a ± 20 % variability range, except for the final measurement. This deviation is likely due to reduced mixing efficiency caused by poorer liquid dispensing control when only a minimal fluid volume remained in the syringe pump. In contrast, the polydispersity index (PDI) exhibited a significant linear decline throughout the cycle, indicating increasingly homogeneous particle distribution.

3.2. Microparticle characterization

After the spray drying process, the yield obtained in the formulation was 57.0 % ± 6.3 %. The DL of AZM within the microparticles was 3.3 % ± 0.5 %, and the EE was 66.6 % ± 10.6 %. Upon reconstitution in aqueous media, the mean particle size was 461.6 nm ± 38.4 nm and particles showed a negative zeta potential of −19.2 mV ± 4.5 mV indicating good colloidal stability.

The morphology of AZM-loaded microparticles is illustrated in Fig. 4. The SEM micrographs revealed a homogeneous appearance with particle sizes around 1 µm (Fig. 4A). No presence of AZM or leucine crystals was detected at the surface of the microparticle indicating an optimal drug encapsulation which was also corroborated by X-ray analysis (Fig. 5). Electron-dense particles < 1 µm in size were observed using TEM (Fig. 4B). The core of the particles showed an intricate fibril mesh

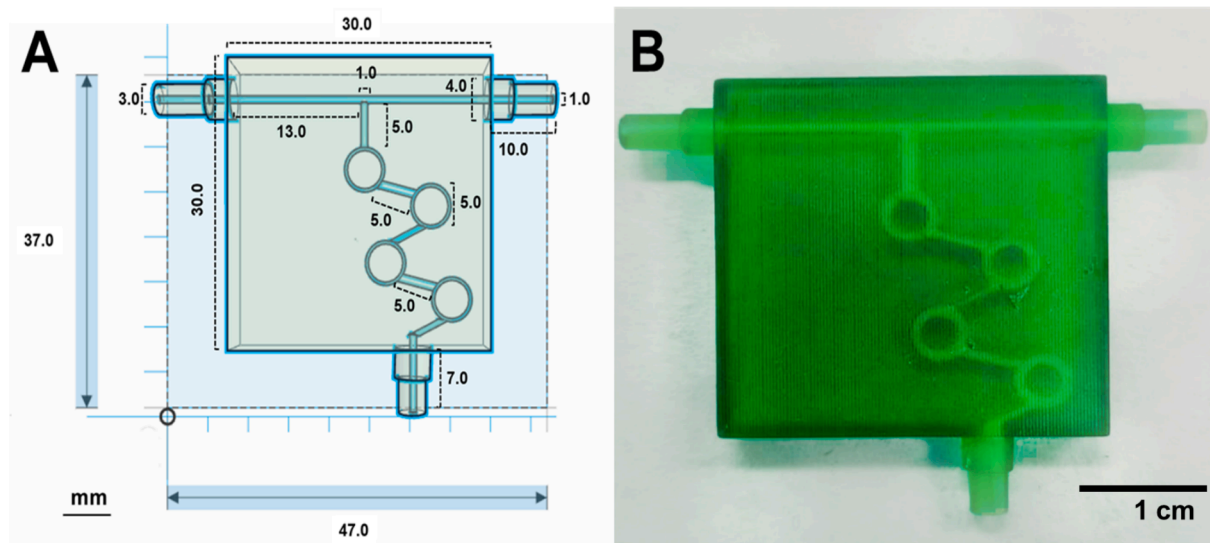


Fig. 1. Design and 3D printed microfluidic device. Key: (A) Geometrical design and dimensions of the 3D microfluidic device, (B) 3D printed microfluidic device by SLA. Photograph obtained from a Xiaomi X3 pro phone (Xiaomi Inc, Beijing, China).

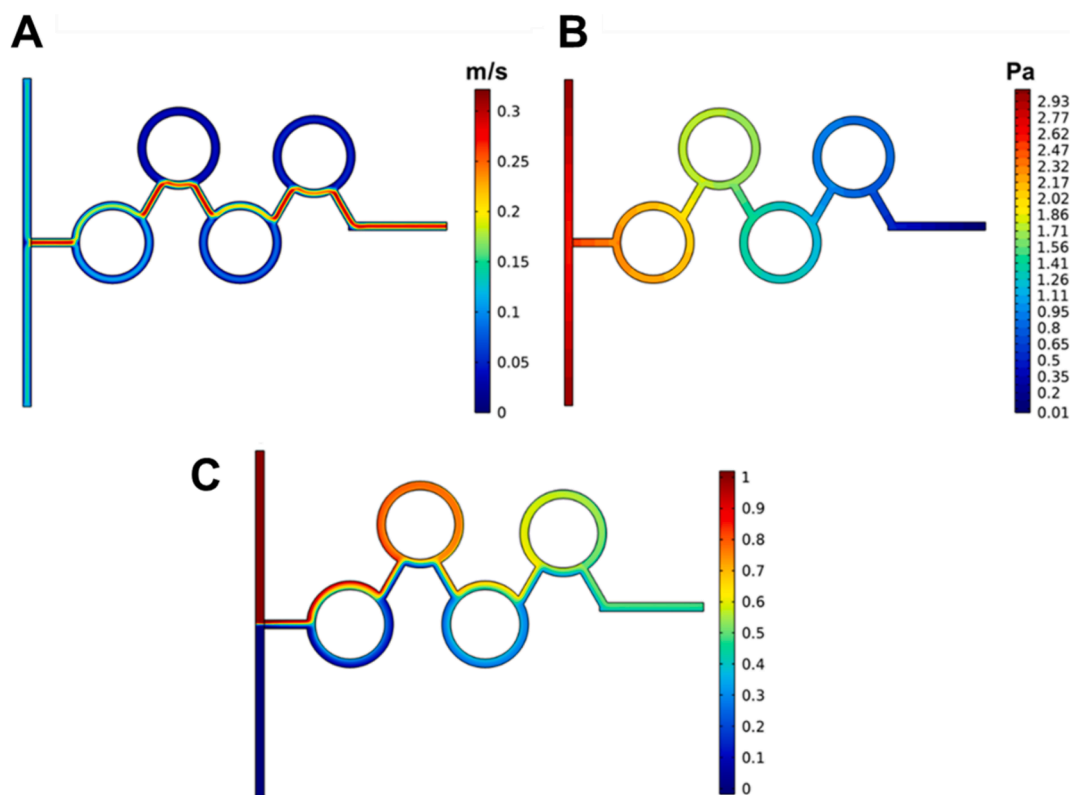


Fig. 2. Contours of mixing in the microfluidic chip after 2 s. Key: (A) velocity magnitude (m/s), (B) Pressure (Pa), (C) Concentration field of the aqueous phase during the mixing period where close to 1 shows unmixed state and 0.5 homogeneously mixed state.

which can be attributed to the ionic complexation occurring between heparin and AZM during the controlled precipitation within the micromixer.

3.3. Solid state characterization of the microparticle formulation

PRXD analysis

PXRD analysis showed distinct Bragg peaks for unprocessed AZM and leucine indicating their crystalline structure while unprocessed

heparin exhibited an amorphous halo (Fig. 5). Peaks of leucine and AZM were still present in the physical mixture. However, the microparticle formulation exhibited a completely amorphous halo, suggesting that the spray-drying process induced full amorphization.

FT-IR analysis

FTIR analysis revealed clear differences between the physical mixture and the microparticles after the spray-dried process (Fig. 6). The physical mixture showed a combined spectral pattern of the individual components, indicating minimal interaction. However, the

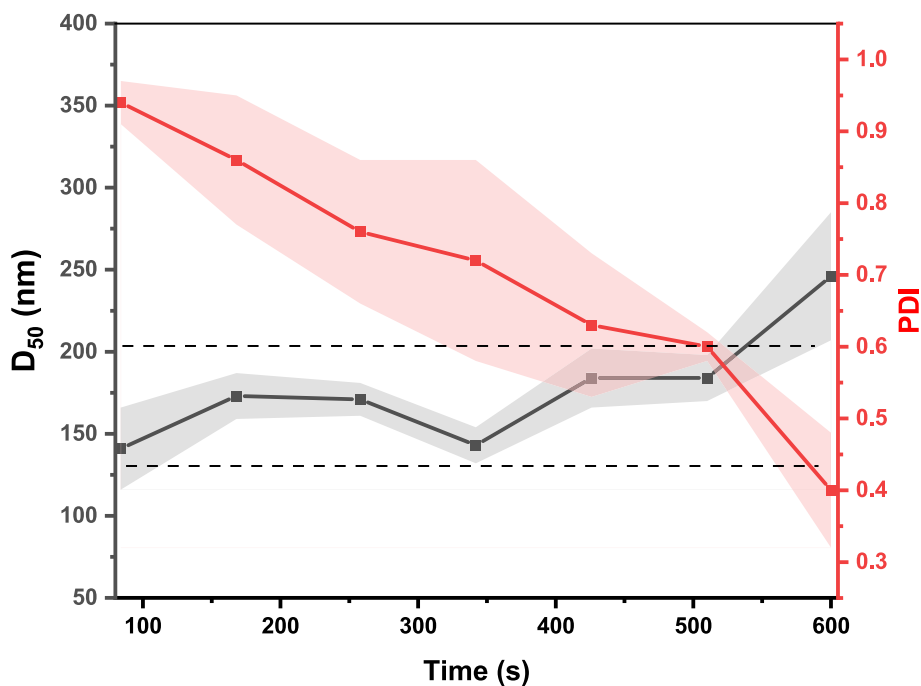


Fig. 3. Impact of the mixing process within the micromixer on particle size (D_{50}) and polydispersity (PDI). Data are expressed as mean \pm SD ($n = 3$). Particle size is expressed in number (D_{50} , nm). The shadowed area corresponds to the SD. Dashed lines represent the average $D_{50} \pm 20\%$ variability.

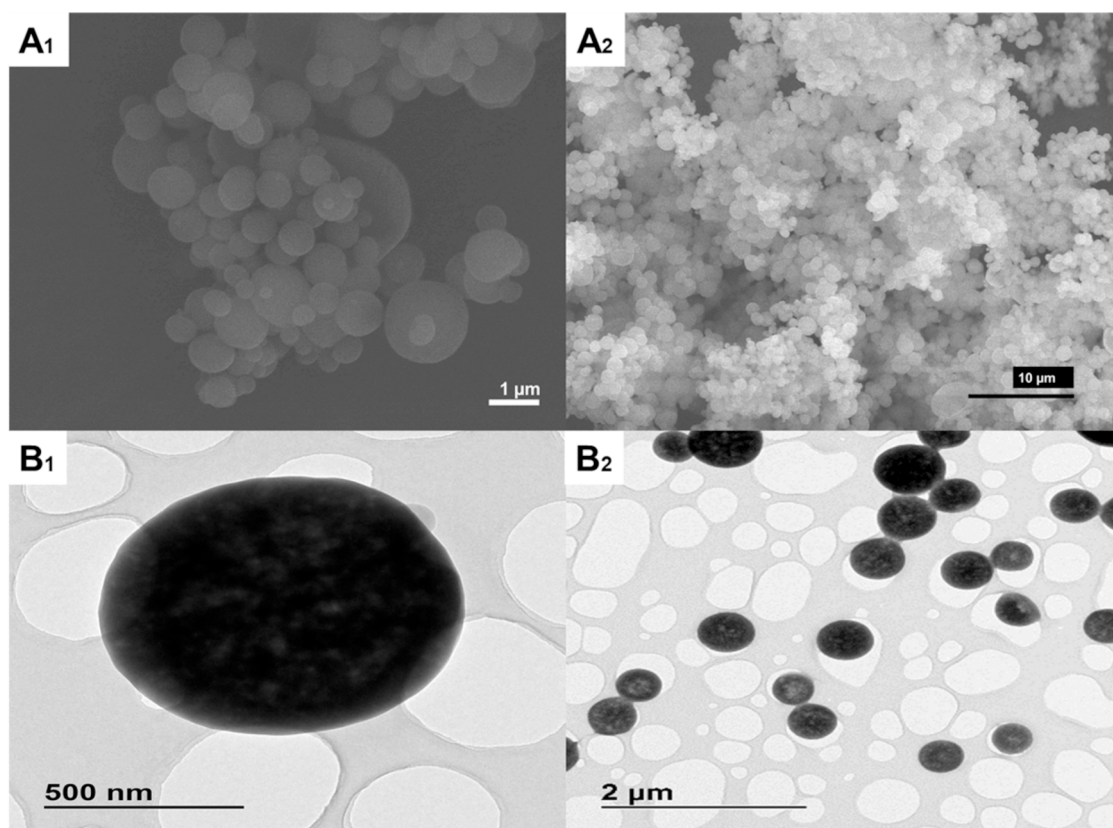


Fig. 4. Morphological analysis. SEM and TEM micrographs were obtained at different magnifications. Key: A) SEM and B) TEM.

microparticle formulation exhibited significant peak shifts and intensity changes, particularly in the $1700\text{ cm}^{-1} - 1500\text{ cm}^{-1}$ region, suggesting H-bond interactions and electrostatic interactions, formed during the nanoprecipitation. In the region between $1300-1000$, well-defined and

sharper peaks were observed for the microparticulate formulation compared to the unprocessed heparin which can be attributed to differences in particle size (Udvardi et al., 2017).

DSC-TGA analysis

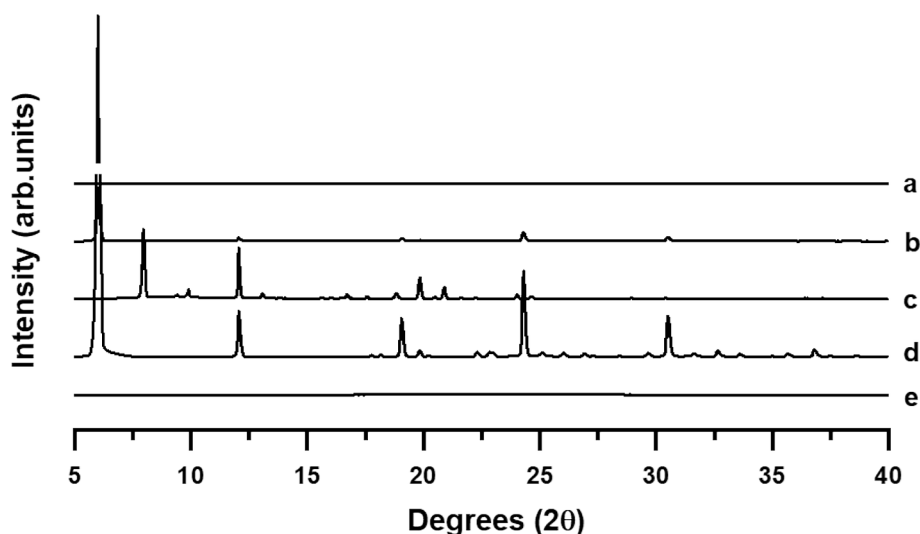


Fig. 5. PXRD analysis. Key: (a) Microparticles, (b) Physical mixture, (c) Unprocessed AZM, (d) Unprocessed Leucine, and (e) Unprocessed Heparin.

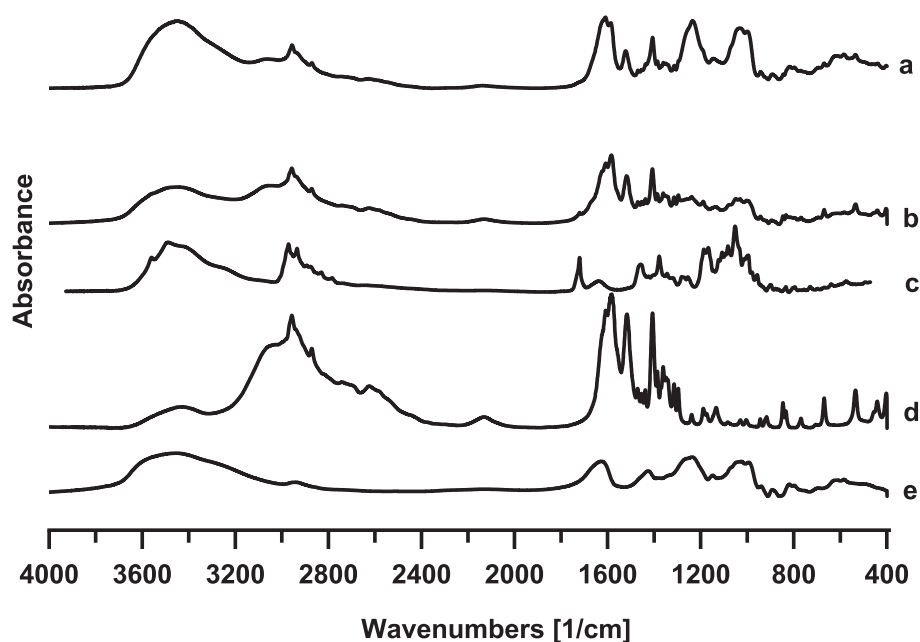


Fig. 6. FTIR analysis. Key: (a) Microparticles, (b) Physical mixture, (c) Unprocessed AZM, (d) Unprocessed Leucine, and (e) Unprocessed Heparin.

Thermal analysis for the formulation and unprocessed materials is shown in Fig. 7. Unprocessed leucine showed a characteristic melting event at $287\text{ }^{\circ}\text{C} \pm 1\text{ }^{\circ}\text{C}$ as well as the azithromycin at $120\text{ }^{\circ}\text{C} \pm 1\text{ }^{\circ}\text{C}$. Unprocessed heparin showed a thermal degradation above $250\text{ }^{\circ}\text{C}$. DSC analysis of the microparticulate formulation demonstrated the absence of endothermic peaks which can be correlated with its amorphous nature (Fig. 7A). The TGA analysis revealed that the microparticulate formulation underwent a rapid initial weight loss ($\sim 20\%$) up to $100\text{ }^{\circ}\text{C}$, attributable to the evaporation of residual solvents after the spray-drying process (Fig. 7B). The microparticulate formulation also exhibited lower thermal stability compared to the physical mixture, starting to degrade from $200\text{ }^{\circ}\text{C}$ onwards.

3.4. *In vitro* assessment of aerodynamic performance

The *in vitro* deposition profile of the formulation is shown in Fig. 8 and summarized in Table 1. While the MMAD was equivalent at both inspiratory flows, the aerodynamic performance analysis of the DPI

formulation revealed distinctive deposition patterns across different flow rates. The FPF $< 5\text{ }\mu\text{m}$ achieved at 30 L/min ($57.2\% \pm 7.4\%$) was significantly higher compared to 60 L/min ($47.9\% \pm 1.3\%$), suggesting superior powder dispersion characteristics at lower inspiratory flow rates.

3.5. *Ex vivo* haemolysis and antibacterial *in vitro* assay

Ex vivo haemolysis on human RBCs (Fig. 9A) exhibited significantly lower haemolytic toxicity for the AZM-loaded microparticle formulation compared to unprocessed AZM within all the tested concentrations. This difference indicates that the encapsulation of AZM within heparin microparticles substantially reduced its haemolytic toxicity. The HC_{50} for the microparticle formulation was 126-fold higher than unprocessed AZM indicating an optimal safety profile.

Antibacterial efficacy studies against *H. influenzae* demonstrated equivalent inhibitory activity for the AZM-loaded microparticles compared to the standard (Fig. 9B). The formulation exhibited an

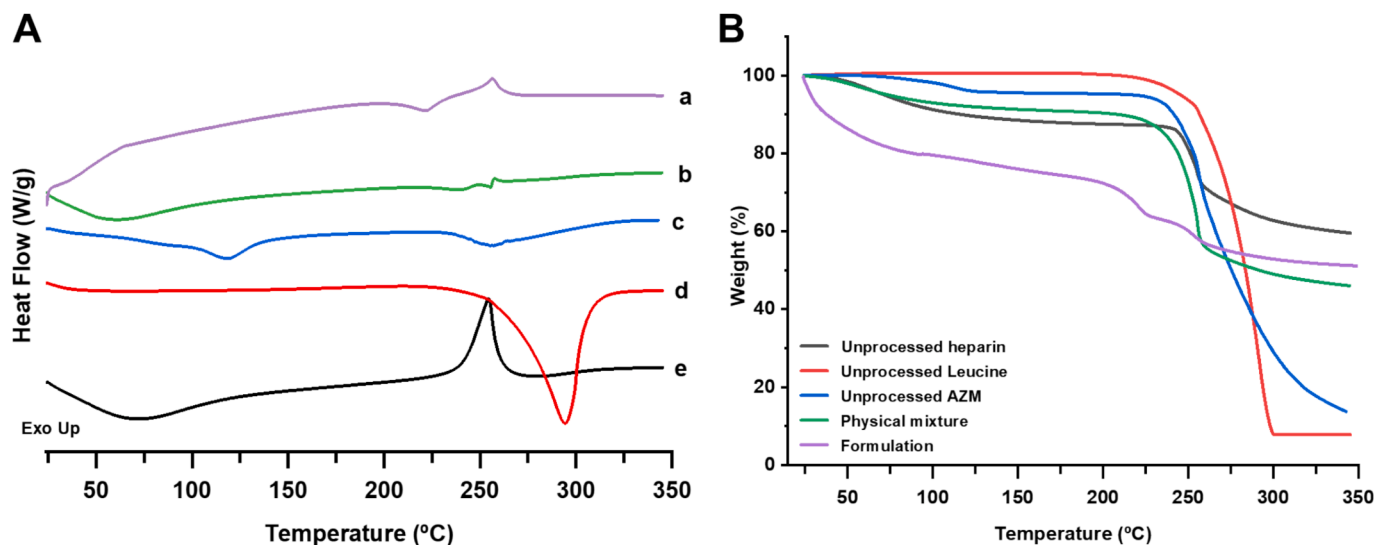


Fig. 7. DSC-TGA analysis. (A) DSC and (B) TGA. Key: (a) Microparticles, (b) Physical mixture, (c) Unprocessed AZM, (d) Unprocessed Leucine, and (e) Unprocessed Heparin.

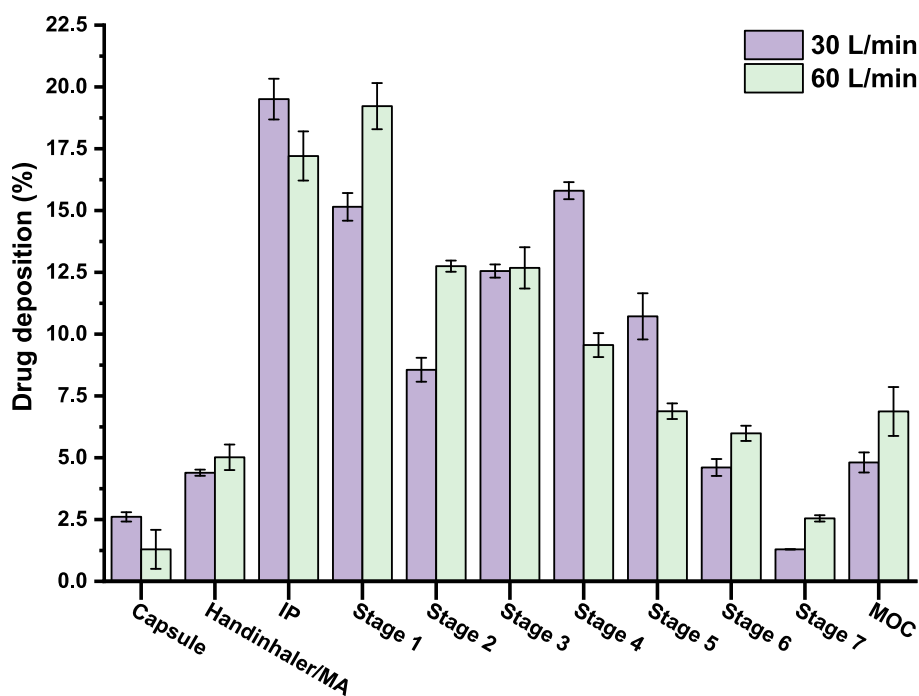


Fig. 8. *In vitro* deposition of AZM in different stages of the NGI. Key: (Handinhaler/MA) device + mouth adaptor (IP) induction port), and (MOC) micro-orifice collector.

Table 1

FPF below 5 μm and 3 μm at 30 L/min and 60 L/min for 8 and 4 s. Data are expressed as mean \pm SD ($n = 3$). Key: MMAD, Mean Mass Aerodynamic Diameter.

Air flow	FPF < 5 μm (%)	FPF < 3 μm (%)	MMAD (μm)
30 L/min	57.2 \pm 7.4	45.8 \pm 5.9	4.0 \pm 1.0
60 L/min	47.9 \pm 1.3	32.8 \pm 0.4	4.1 \pm 0.1

inhibition halo of 21.13 mm \pm 0.38 mm, which was comparable to that of the commercial AZM disk (21.00 mm \pm 0.56 mm). No statistical significance ($p > 0.05$) was observed, indicating that the AZM-microparticles formulation maintained antimicrobial efficacy being

able to diffuse from the carrier.

3.6. *In vitro* cytotoxicity MTT assays

Fig. 10 shows the effect of the AZM-loaded microparticles on Calu-3 and J774A.1 cell viability. In Calu-3 cells, cell viability remained high (> 94%) at concentrations up to 25 $\mu\text{g}/\text{mL}$, indicating a favorable safety profile and minimal cytotoxicity. However, a moderate but significant decrease in cell viability was observed at the highest tested concentration of 50 $\mu\text{g}/\text{mL}$, reducing viability to 64.5% (Fig. 10A). Microscopic examination supported these findings, revealing minimal morphological alterations at 25 $\mu\text{g}/\text{mL}$, while pronounced morphological changes and a reduction in cell number were observed after incubation with 50 $\mu\text{g}/\text{mL}$

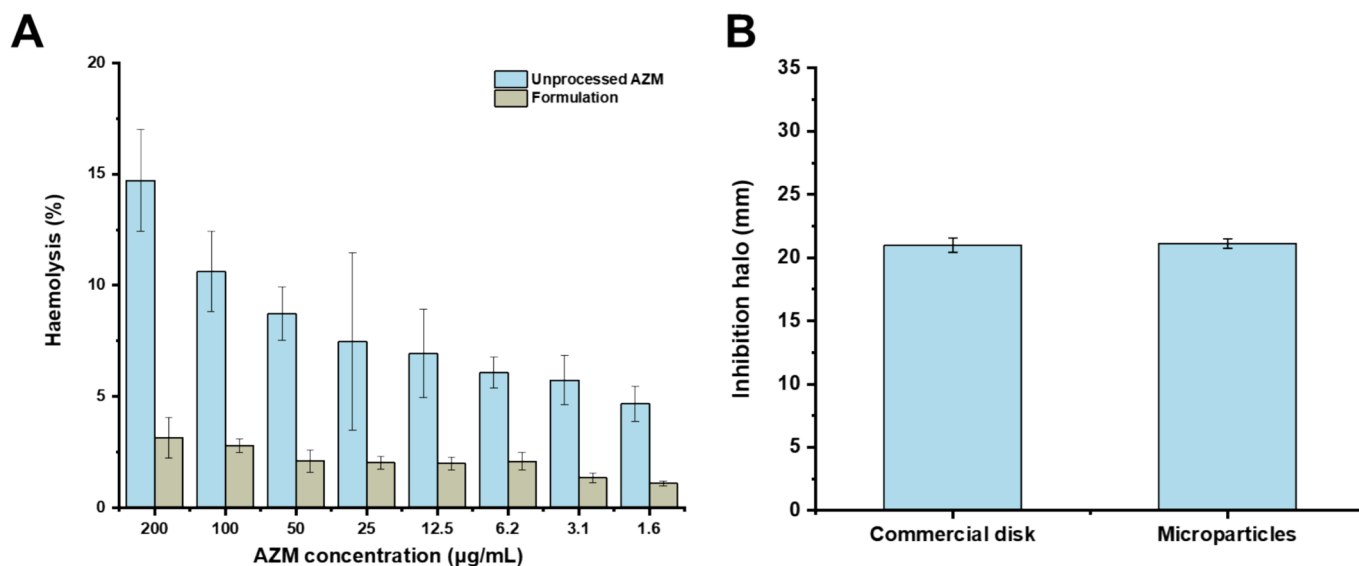


Fig. 9. A) *In vitro* haemolysis of AZM-loaded microparticle formulation. Data are expressed as mean \pm SD ($n = 3$). B) *In vitro* antibacterial assay against *H. influenzae*. Data are expressed as mean \pm SD ($n = 5$).

AZM-loaded microparticles. (Fig. 10C). On the other hand, the AZM formulation had no effect on the viability of J774A.1 cells at any assayed concentrations (from 0.1 to 50 $\mu\text{g/mL}$) (Fig. 10B).

4. Discussion

The integration of microfluidics with spray drying has shown to be a promising approach for the manufacture of inhalable microparticles. This process enables the continuous manufacture of dry powder inhalers which, to the best of our knowledge, has not been previously described. This approach has the potential to revolutionize the current landscape of industrial strategies for fabricating dry powder inhalers. The integration of microfluidics allows for precisely controlled precipitation making it easier to tune the desired particle size while the spray-drying ensures a suitable drying step preventing aggregation.

Microfluidic micromixers have been previously used for drug nano-encapsulation using carbohydrates. Tran *et al.* (2012) (Tran *et al.*, 2012) developed a microfluidic chip that rapidly synthesized uniform heparin-folic acid-retinoic acid nanoparticles (130 nm, PDI = 0.101) with high drug coupling ratios (17 drug molecules per heparin chain) via ionic complexation. The microfluidic chip was designed with a solvent-resistant fluoropolymer, forming a 500 μm wide, 50 μm high, and 40 cm long microchannel with two inlets and one outlet. This geometry enabled precise control over reagent mixing and residence time, facilitating efficient drug conjugation to heparin chains. Flow rates were adjusted to control reaction time using a dual syringe pump, solutions were introduced at identical flow rates, achieving residence times of 1 to 2.5 min. The microfluidic approach significantly reduced the reaction time from days to minutes compared to bulk synthesis. The nanoparticles produced by the microfluidic chip exhibited a 37 % increase in cellular uptake with a 20 % increase in cytotoxicity against cancer cells compared to their bulk-synthesized counterparts.

In our work, the microfluidic design was optimized based on CFD simulations along with experimental validation to enhance mixing efficiency and particle engineering. The T-junction was selected to ensure rapid initial contact between the organic and aqueous phases, promoting early-stage diffusion and minimizing phase separation. The four interconnected circular rings (5 mm diameter, 1 mm channel width) positioned at a 45° angle were designed to induce chaotic advection, which is crucial for efficient mixing in laminar flow regimes. The 1 mm channel diameter was chosen to balance flow resistance and Reynolds number, ensuring effective mixing while maintaining a manageable

pressure drop. The overall dimensions (3.7 cm \times 4.7 cm \times 0.6 cm) were constrained by the resolution and build volume of the 3D printer while ensuring practical handling and integration with fluidic connections. These design choices significantly impact particle quality by reducing concentration gradients, controlling shear rates, and preventing aggregation, ultimately leading to uniform and well-defined particles.

The geometry of the microfluidic micromixer was optimized to achieve an enhanced mixing index of 0.943 which combined with a low total flow rate (10 mL/min), a larger particle size for optimal lung delivery was targeted. Ionic complexation is also expected to occur during the controlled precipitation step considering that at physiological pH, heparin is negatively charged while AZM is the opposite. The coupling with spray drying resulted in a high yield (57 %), DL (3.3 %) and EE (66 %) considering the hydrophilic nature of the drug. Previous reports on AZM encapsulation exhibited much lower yields and EE (< 50 %) (Abo-Zeid *et al.*, 2022; Li *et al.*, 2012). Also, particles obtained by combining the nanoprecipitation within the micromixer with the spray drying resulted in a smaller size with a more homogenous particle size distribution with greater deposition in the lungs compared to direct spray drying (Anaya *et al.*, 2025).

DPI performance is influenced by device resistance, which determines the relationship between inspiratory pressure and flow rate. Higher-resistance DPIs result in lower flow rates at the same inspiratory effort, affecting aerosolization and deposition efficiency. The Handihaler device, for example, delivers dry powder at flow rates as low as 20 L/min. In COPD patients with severely compromised lung function (correlated with a mean Forced Expiratory Volume in 1 s of 1.02 L), the median peak inspiratory flow through the Handihaler was 30.0 L/min (range 20.4–45.6 L/min) (SPIRIVA® HANDIHALER). These findings align with data showing that at a lower flow rate of 30 L/min, fine particle fractions (FPF < 5 μm : 57.2 % \pm 7.4 %; FPF < 3 μm : 45.8 % \pm 5.9 %) suggest improved deep lung deposition, particularly in the alveolar region due to enhanced diffusion. This is crucial for patients with reduced inspiratory capacity, such as those with COPD or asthma, as lower flow rates enhance gravitational settling and minimize exhalation losses. Given the variability in drug delivery based on inspiratory flow, optimizing inhaler design for patients with compromised respiratory function remains essential (Clark *et al.*, 2020; Vartiainen *et al.*, 2023).

A significant advantage of this formulation is its lower susceptibility to inspiratory flow rates compared to other formulations (Gauani *et al.*, 2023; Chavan and Dalby, 2002; Wang *et al.*, 2024). No significant

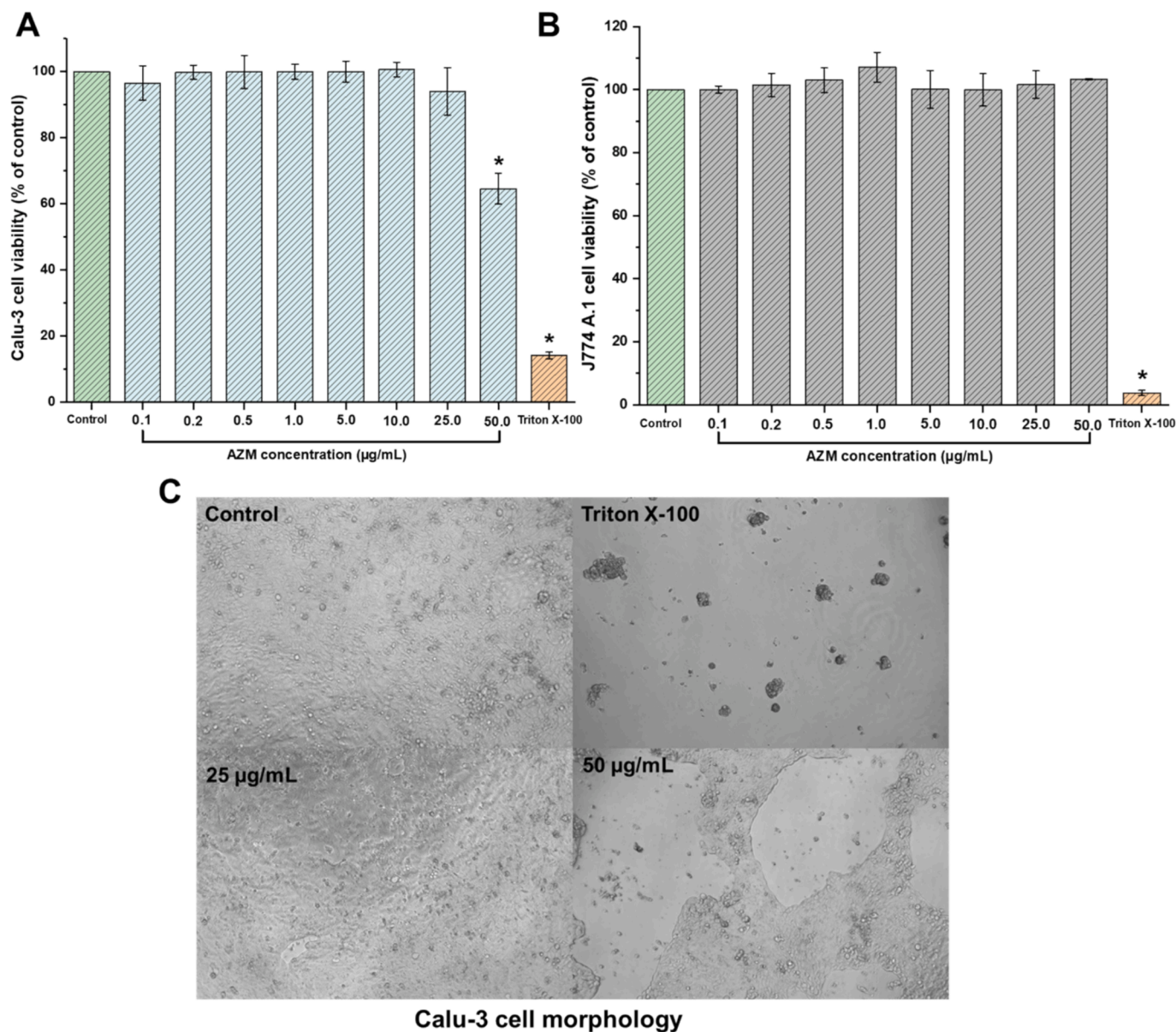


Fig. 10. Effect on cell viability using MTT assay. A) Calu-3 cells, and B) J774A.1 cells. Cells were treated with the formulation at AZM concentrations ranging from 0.1 µg/mL to 50.0 µg/mL for 24 h. Triton X-100 was used as a positive cytotoxic control. Data are expressed as mean ± SD ($n = 6$). * $p < 0.05$ vs control. C) **Effect on Calu-3 cell morphology.** Images were obtained with a Leica microscope at x10 magnification at 25 µg/mL and 50 µg/mL AZM concentration at 24 h.

differences were observed in the MMAD but a greater FPF was obtained for the lower inspiratory airflow tested. The integration of microfluidic technology with spray drying allows for the precise control of droplet formation, which is essential for achieving uniform and smaller particle sizes suitable for alveolar deposition ($< 3 \mu\text{m}$) (Kartanas et al., 2020).

Particle size plays a critical role in determining the deposition, distribution, and efficacy of drugs delivered to the lungs. Particles smaller than 5 µm, particularly those between 0.5 µm – 2 µm, are ideal for achieving optimal lung deposition and alveolar concentration (Dudhat and Patel, 2022). These outcomes are consistent with established deposition mechanisms, such as inertial impaction and gravitational sedimentation, which are influenced by particle size and aerodynamic diameter. Notably, particles in the 0.1 µm – 1.5 µm range exhibit minimal sensitivity to flow rate (500 mL/s – 2000 mL/s) but significant responsiveness to breath-holding duration (Min et al., 2023). This can be challenging considering the different inspiratory capacities of patients suffering from respiratory diseases. Micron-sized particles, such as mesoporous silica particles (MSPs), offer controlled drug release,

enhanced efficiency, and stability (Pacheco et al., 2024; van der Zwaan et al., 2024). Deposition profiles are intricately linked to individual lung characteristics and breathing patterns (Rissler et al., 2023; Barrio-Perotti et al., 2023). The balance between mucociliary advection and diffusion in the mucus layer affects drug availability across lung regions, with breath control techniques enhancing deep lung delivery for 0.5 µm – 2 µm aerosols (Chakravarty et al., 2022). Precise particle engineering is essential to maximize therapeutic efficacy, minimize side effects, and ensure reliable drug delivery making the 3D-printed micromixers coupled with spray drying a useful tool for tuning particle size. In this work, we have demonstrated that controlling particle precipitation using microfluidic micromixers coupled with spray drying can provide us with a feasible tool for this purpose.

Haemolysis testing serves as a critical *in vitro* method for evaluating both the membrane-damaging potential and biocompatibility of inhaled particles in biological systems, particularly in the alveolar region where systemic exposure to red blood cells occurs. Our study demonstrated that AZM-loaded heparin microparticles exhibited lower haemolytic

toxicity compared to the unencapsulated drug (Shi et al., 2012; Thakare et al., 2024). The minimal haemolytic activity observed under tested conditions supports the safety profile of the developed spray-dried formulation, validating its suitability for pharmaceutical applications and safety for pulmonary administration.

In pulmonary drug delivery, the relationship between epithelial lining fluid (ELF) volume and drug concentration is crucial for ensuring therapeutic efficacy. ELF constitutes approximately 0.39 % of total lung capacity, with volumes ranging from 23.4 mL in healthy adults to 15.6 mL in individuals with compromised pulmonary function (Rodvold et al., 2011; Drwiega and Rodvold, 2022; Chinard, 1992). In our study, we targeted concentrations of 20 µg/mL of AZM in ELF, exceeding by 5-fold the reported epidemiological cut-offs (ECOFFs) in *H. influenzae* for AZM (4 mg/L (EUCAST) while maintaining higher lung cell viability (> 94 %), without toxicity on macrophage cells. Bearing in mind a drug loading of 3.3 % and an FPF of 57.2 %, the inhalation of 25 mg of dry powder would result in 472 µg of AZM delivered to the lung. Assuming 23.4 mL of ELF, the AZM concentration in the lung would be 20 µg/mL which is well above the ECOFF. The final regime of administration should be adjusted based on the pharmacokinetic profile of AZM in the lung.

5. Conclusion

This work introduces an innovative approach to pulmonary drug delivery by combining 3D-printed microfluidic devices with spray-drying technology to produce AZM microparticles for efficient pulmonary delivery. This study demonstrates the integration of advanced technologies to enhance pulmonary drug deposition, showing promise for improved therapeutic outcomes. This combined approach allows for precise control over particle size, distribution, and encapsulation efficiency while promoting enhanced mixing and yield. The scalability, reproducibility, and rapid process development capabilities of this integrated approach facilitate the optimization of formulation parameters and the production of stable, customizable particles with improved aerodynamic properties for lung delivery.

CRedit authorship contribution statement

Brayan J. Anaya: Writing – original draft, Visualization, Validation, Software, Methodology, Investigation, Formal analysis, Data curation. **Aytug Kara:** Visualization, Formal analysis, Data curation. **Rafaela Raposo:** Methodology. **Diego F. Tirado:** Writing – review & editing, Validation, Supervision, Resources, Methodology, Formal analysis, Data curation, Conceptualization. **Aikaterini Lalatsa:** Writing – review & editing, Visualization, Supervision, Methodology, Investigation, Formal analysis. **Elena González-Burgos:** Writing – review & editing, Visualization, Validation, Supervision, Resources, Methodology, Investigation, Formal analysis, Data curation, Conceptualization. **D.R. Serrano:** Writing – review & editing, Visualization, Validation, Supervision, Resources, Project administration, Methodology, Investigation, Funding acquisition, Formal analysis, Data curation, Conceptualization.

Declaration of competing interest

The authors declare the following financial interests/personal relationships which may be considered as potential competing interests: Dolores R Serrano reports financial support was provided by Spanish Ministry of Science and Innovation. Diego F. Tirado reports financial support was provided by National University of Colombia - La Paz. Brayan J Anaya reports financial support was provided by Colombia Ministry of Science Technology and Innovation. If there are other authors, they declare that they have no known competing financial interests or personal relationships that could have appeared to influence the work reported in this paper.

Acknowledgments

Brayan J. Anaya thanks the Ministerio de Ciencia Tecnología e Innovación (MinCiencias) of Colombia, Call No. 885 of 2020, for the doctoral scholarship. This study has also been partially funded by the Spanish Ministry of Science and Innovation and Agencia Estatal de Investigación (award PID2021-126310OA-I00 to Dolores Serrano) and the Universidad Nacional de Colombia (project reference 58990).

Appendix A. Supplementary data

Supplementary data to this article can be found online at <https://doi.org/10.1016/j.ijpharm.2025.125493>.

Data availability

Data will be made available on request.

References

- Abo-Zeid, Y., et al., 2022. Antimicrobial activity of azithromycin encapsulated into PLGA NPs: a potential strategy to overcome efflux resistance. *Antibiotics* 11 (11), 1623.
- Al-Hakkani, M.F., 2019. A rapid, developed and validated RP-HPLC method for determination of azithromycin. *SN Appl. Sci.* 1 (3), 222.
- Al-Zoubi, N., et al., 2021. Spray drying for direct compression of pharmaceuticals. *Processes* 9 (2), 267.
- Anaya, B.J., et al., 2023. Engineering of 3D printed personalized polypills for the treatment of the metabolic syndrome. *Int. J. Pharm.* 642, 123194.
- Anaya, B.J., et al., 2024. Heparin-azithromycin microparticles show anti-inflammatory effects and inhibit SARS-CoV-2 and bacterial pathogens associated to lung infections. *Carbohydr. Polym.*, 122930
- Anaya, B.J., et al., 2025. Heparin-azithromycin microparticles show anti-inflammatory effects and inhibit SARS-CoV-2 and bacterial pathogens associated to lung infections. *Carbohydr. Polym.* 348 (Pt B), 122930.
- Anaya, B.J., et al., 2025. Heparin-azithromycin microparticles show anti-inflammatory effects and inhibit SARS-CoV-2 and bacterial pathogens associated to lung infections. *Carbohydr. Polym.* 348, 122930.
- Barrio-Perotti, R., et al., 2023. Predicting particle deposition using a simplified 8-path in silico human lung prototype. *J. Breath Res.* 17 (4), 046002.
- Baumann, J.M., Adam, M.S., Wood, J.D., 2021. Engineering advances in spray drying for pharmaceuticals. *Annu. Rev. Chem. Biomol. Eng.* 12 (1), 217–240.
- Celi, S.S., et al., 2023. Co-delivery of a high dose of amphotericin b and itraconazole by means of a dry powder inhaler formulation for the treatment of severe fungal pulmonary infections. *Pharmaceutics* 15 (11), 2601.
- Chakravarty, A., et al., 2022. Pulmonary drug delivery and retention: A computational study to identify plausible parameters based on a coupled airway-mucus flow model. *PLoS Comput. Biol.* 18 (6), e1010143.
- Chandel, A., et al., 2019. Recent advances in aerosolised drug delivery. *Biomed. Pharmacother.* 112, 108601.
- Chavan, V., Dalby, R., 2002. Novel system to investigate the effects of inhaled volume and rates of rise in simulated inspiratory air flow on fine particle output from a dry powder inhaler. *AAPS PharmSci* 4, 7–12.
- Chen, X., Shen, J., 2017. Simulation and experimental analysis of a SAR micromixer with F-shape mixing units. *Anal. Methods* 9 (12), 1885–1890.
- Chinard, F.P., 1992. Quantitative assessment of epithelial lining fluid in the lung. *Am. J. Physiol.-Lung Cell. Mol. Physiol.* 263 (6), L617–L618.
- Clark, A.R., Weers, J.G., Dhand, R., 2020. The confusing world of dry powder inhalers: it is all about inspiratory pressures, not inspiratory flow rates. *J. Aerosol Med. Pulm. Drug Deliv.* 33 (1), 1–11.
- Costanzo, L., et al., 2020. Coagulopathy, thromboembolic complications, and the use of heparin in COVID-19 pneumonia. *J. Vasc. Surg. Venous Lymphat. Disord.* 8 (5), 711–716.
- de Pablo, E., et al., 2017. Nebulised antibiotherapy: conventional versus nanotechnology-based approaches, is targeting at a nano scale a difficult subject? *Ann. Translational Med.* 5 (22).
- de Pablo, E., et al., 2023. Targeting lung macrophages for fungal and parasitic pulmonary infections with innovative amphotericin B dry powder inhalers. *Int. J. Pharm.* 635, 122788.
- Drwiega, E.N., Rodvold, K.A., 2022. Penetration of antibacterial agents into pulmonary epithelial lining fluid: an update. *Clin. Pharmacokinet.* 61 (1), 17–46.
- Dudhat, K.R., Patel, H.V., 2022. Influence of particle size and particle deposition of inhaled medication in lung disease: a comprehensive review. *Int. J. Pharm. Sci. Drug Res.* 141–157.
- EUCAST Clinical breakpoints - breakpoints and guidance. Available at: https://www.eucast.org/clinical_breakpoints. Date: 01/02/2025.
- Gauani, H., et al., 2023. Effect of inhalation profile on delivery of treprostinil palmitil inhalation powder. *Pharmaceutics* 15 (3), 934.
- Gholizadeh-Hashjin, A., et al., 2024. Compatibility study of formoterol fumarate-lactose dry powder inhalation formulations: Spray drying, physical mixture and commercial DPIs. *J. Drug Delivery Sci. Technol.* 95, 105538.

- Gondhale-Karpe, P., 2023. Novel Techniques in Pulmonary Drug Delivery Systems. In: *Novel Technologies in Biosystems, Biomedical & Drug Delivery*. Springer, pp. 221–239.
- Gualdoni, G.A., et al., 2015. Azithromycin inhibits IL-1 secretion and non-canonical inflammasome activation. *Sci. Rep.* 5 (1), 12016.
- Haque, S., et al., 2018. The applications of 3D printing in pulmonary drug delivery and treatment of respiratory disorders. *Curr. Pharm. Des.* 24 (42), 5072–5080.
- Ibrahim, M., Verma, R., Garcia-Contreras, L., 2015. Inhalation drug delivery devices: technology update. *Med. Devices: Evidence Res.* 131–139.
- ICH, E., *Impurities: Guidelines for residual solvents Q3C (R5)*. 2011, ICH Geneva, Switzerland.
- Javaid, M.U., Cheema, T.A., Park, C.W., 2017. Analysis of passive mixing in a serpentine microchannel with sinusoidal side walls. *Micromachines* 9 (1), 8.
- Javaid, M.U., Cheema, T.A., Park, C.W., 2018. Analysis of passive mixing in a serpentine microchannel with sinusoidal side walls. *Micromachines* 9 (1), 8.
- Joelsson, J.P., et al., 2020. Azithromycin ameliorates sulfur dioxide-induced airway epithelial damage and inflammatory responses. *Respir. Res.* 21, 1–11.
- Jones, R.N., et al., 1994. Validation of NCCLS macrolide (azithromycin, clarithromycin, and erythromycin) interpretive criteria for *Haemophilus influenzae* tested with the Haemophilus test medium. *Diagn. Microbiol. Infect. Dis.* 18 (4), 243–249.
- Kara, A., et al., 2021. Engineering 3D printed microfluidic chips for the fabrication of nanomedicines. *Pharmaceutics* 13 (12), 2134.
- Kara, A., et al., 2023. Continuous manufacturing of cocrystals using 3d-printed microfluidic chips coupled with spray coating. *Pharmaceuticals* 16 (8), 1064.
- Kara, A., et al., 2023. 3D printing technologies for personalized drug delivery. In: *Emerging Drug Delivery and Biomedical Engineering Technologies*. CRC Press, pp. 31–47.
- Kartanas, T., et al., 2020. Mechanism of droplet-formation in a supersonic microfluidic spray device. *Appl. Phys. Lett.* 116 (15).
- Kjellberg, S., et al., 2024. Impaired function in the lung periphery following COVID-19 is associated with lingering breathing difficulties. *Physiol. Rep.* 12 (2), e15918.
- Knap, K., et al., 2023. Inhalable microparticles as drug delivery systems to the lungs in a dry powder formulations. *Regener. Biomater.* 10 rbac099.
- Kuga, K., et al., 2023. Effect of transient breathing cycle on the deposition of micro and nanoparticles on respiratory walls. *Comput. Methods Programs Biomed.* 236, 107501.
- Kumar, R., et al., 2022. Nanotechnology-assisted metered-dose inhalers (MDIs) for high-performance pulmonary drug delivery applications. *Pharm. Res.* 39 (11), 2831–2855.
- Leal, T., et al., 2016. Azithromycin attenuates *Pseudomonas*-induced lung inflammation by targeting bacterial proteins secreted in the cultured medium. *Front. Immunol.* 7, 499.
- Lechanteur, A., Evrard, B., 2020. Influence of composition and spray-drying process parameters on carrier-free DPI properties and behaviors in the lung: A review. *Pharmaceutics* 12 (1), 55.
- Li, X., et al., 2012. Encapsulation of azithromycin into polymeric microspheres by reduced pressure-solvent evaporation method. *Int. J. Pharm.* 433 (1–2), 79–88.
- Liu, H., et al., 2023. Computational investigation of flow characteristics and particle deposition patterns in a realistic human airway model under different breathing conditions. *Respir. Physiol. Neurobiol.* 314, 104085.
- Malamatari, M., et al., 2020. Spray drying for the preparation of nanoparticle-based drug formulations as dry powders for inhalation. *Processes* 8 (7), 788.
- Mangiafico, M., Caff, A., Costanzo, L., 2022. The role of heparin in COVID-19: an update after two years of pandemics. *J. Clin. Med.* 11 (11), 3099.
- Marple, V.A., et al., 2003. Next generation pharmaceutical impactor (a new impactor for pharmaceutical inhaler testing). Part I: Design. *J. Aerosol Med.* 16 (3), 283–299.
- Min, H.J., Stride, E.P., Payne, S.J., 2023. In silico investigation of the effect of particle diameter on deposition uniformity in pulmonary drug delivery. *Aerosol Sci. Tech.* 57 (4), 318–328.
- Oliver, M.E., Hinks, T.S., 2021. Azithromycin in viral infections. *Rev. Med. Virol.* 31 (2), e2163.
- Ongoren, B., et al., 2024. Leveraging 3D-printed microfluidic micromixers for the continuous manufacture of melatonin loaded SNEDDS with enhanced antioxidant activity and skin permeability. *Int. J. Pharm.*, 124536
- Ongoren, B., et al., 2024. Leveraging 3D-printed microfluidic micromixers for the continuous manufacture of melatonin loaded SNEDDS with enhanced antioxidant activity and skin permeability. *Int. J. Pharm.* 663, 124536.
- Orea-Tejeda, A., et al., 2023. Dynapenia and sarcopenia in post-COVID-19 syndrome hospitalized patients are associated with severe reduction in pulmonary function. *J. Clin. Med.* 12 (20), 6466.
- Osouli-Bostanabad, K., et al., 2022. Microfluidic manufacture of lipid-based nanomedicines. *Pharmaceutics* 14 (9), 1940.
- Ossebaard, H.C., et al., 2021. Turning green: the impact of changing to more eco-friendly respiratory healthcare. A carbon and cost analysis of Dutch prescription data. *medRxiv*, p. 2021.11.20.21266571.
- Pacheco, J.E.C., et al., 2024. Inhalable porous particles as dual micro-nano carriers demonstrating efficient lung drug delivery for treatment of tuberculosis. *J. Control. Release* 369, 231–250.
- Patel, A., et al., Azithromycin in combination with ceftriaxone reduces systemic inflammation and provides survival benefit in a murine model of polymicrobial sepsis. *Antimicrobial agents and chemotherapy*, 2018. 62(9): p. 10.1128/aac.00752-18.
- Patil, A., et al., 2023. Combined microfluidics and drying processes for the continuous production of micro-/nanoparticles for drug delivery: a review. *Drying Technol.* 41 (10), 1533–1568.
- Pineros, I., et al., 2017. Analgesic and anti-inflammatory controlled-released injectable microemulsion: Pseudo-ternary phase diagrams, in vitro, ex vivo and in vivo evaluation. *Eur. J. Pharm. Sci.* 101, 220–227.
- Pugia, M.J., et al., 2005. Microfluidic tool box as technology platform for hand-held diagnostics. *Clin. Chem.* 51 (10), 1923–1932.
- Rahman, M., et al., 2022. Numerical study of nano and micro pollutant particle transport and deposition in realistic human lung airways. *Powder Technol.* 402, 117364.
- Ribeiro Baptista, B., et al., 2022. Identification of factors impairing exercise capacity after severe COVID-19 pulmonary infection: a 3-month follow-up of prospective COVulnerability cohort. *Respir. Res.* 23 (1), 68.
- Rissler, J., et al., 2023. An experimental study on lung deposition of inhaled 2 µm particles in relation to lung characteristics and deposition models. *Part. Fibre Toxicol.* 20 (1), 40.
- Rodvold, K.A., George, J.M., Yoo, L., 2011. Penetration of anti-infective agents into pulmonary epithelial lining fluid: focus on antibacterial agents. *Clin. Pharmacokinet.* 50, 637–664.
- Santamaría, K.J., et al., 2024. Engineering 3D printed gummies loaded with metformin for paediatric use. *Gels* 10 (10), 620.
- Saris, A., et al., 2022. The azithromycin pro-drug CSY5669 boosts bacterial killing while attenuating lung inflammation associated with pneumonia caused by methicillin-resistant staphylococcus aureus. *Antimicrob. Agents Chemother.* 66 (9) e02298-21.
- Segal, L.N., et al., 2017. Randomised, double-blind, placebo-controlled trial with azithromycin selects for anti-inflammatory microbial metabolites in the emphysematous lung. *Thorax* 72 (1), 13–22.
- Serrano, D.R., et al., 2015. Oral particle uptake and organ targeting drives the activity of amphotericin B nanoparticles. *Mol. Pharm.* 12 (2), 420–431.
- Serrano, D., et al., 2023. 3D printing technologies in personalized medicine, nanomedicines, and biopharmaceuticals. *Pharmaceutics* 15.
- Shi, J., et al., 2012. Hemolytic properties of synthetic nano-and porous silica particles: the effect of surface properties and the protection by the plasma corona. *Acta Biomater.* 8 (9), 3478–3490.
- Smith, L., et al., 2018. Orally bioavailable and effective buparvaquone lipid-based nanomedicines for visceral leishmaniasis. *Mol. Pharm.* 15 (7), 2570–2583.
- SPIRIVA® HANDIHALER® (tiotropium bromide inhalation powder) for oral inhalation use. Available at: <https://content.boehringer-ingenelheim.com/DAM/7e63d875-6ffb-407d-a561-af1e012045e5/spiriva%20handihaler-us-pi.pdf>. Accessed date: 01/02/2025.
- Ta, B.Q., et al., 2015. Geometric effects on mixing performance in a novel passive micromixer with trapezoidal-zigzag channels. *J. Micromech. Microeng.* 25 (9), 094004.
- Technology, N.I.O.S.a. Thermophysical Properties of Fluid Systems. [cited 2023 11]; Available from: <https://webbook.nist.gov/chemistry/liquid/>.
- Thakare, P., et al., 2024. Exploring the potential of three-layered self-assembled biomaterial-based dry powder inhaler for enhanced structural integrity and lung deposition of bioactive Lysozyme. *BioNanoScience* 14 (3), 3341–3354.
- Tran, T.H., et al., 2012. Microfluidic approach for highly efficient synthesis of heparin-based bioconjugates for drug delivery. *Lab Chip* 12 (3), 589–594.
- Tree, J.A., et al., 2021. Unfractionated heparin inhibits live wild type SARS-CoV-2 cell infectivity at therapeutically relevant concentrations. *Br. J. Pharmacol.* 178 (3), 626–635.
- Tyagi, N., et al., 2024. 3D printing technology in the pharmaceutical and biomedical applications: a critical review. *Biomed. Mater. Devices* 2 (1), 178–190.
- Udvardi, B., et al., 2017. Effects of particle size on the attenuated total reflection spectrum of minerals. *Appl. Spectrosc.* 71 (6), 1157–1168.
- van der Zwaan, I., et al., 2024. Influence of particle diameter on aerosolization performance and release of budesonide loaded mesoporous silica particles. *Eur. J. Pharm. Sci.*, 106828
- Vartiainen, V.A., et al., 2023. High inhaler resistance does not limit successful inspiratory maneuver among patients with asthma or COPD. *Expert Opin. Drug Deliv.* 20 (3), 385–393.
- Wang, B., et al., 2024. Effect of airflow rate on droplet deposition of an impinging-jet inhaler in the human respiratory tract. *Int. J. Pharm.* 661, 124408.
- Welton, T., 2015. Solvents and sustainable chemistry. *Proc. R. Soc. A: Math., Phys. Eng. Sci.*, 2015. 471(2183): p. 20150502.
- Wu, K., et al., 2022. Recent progress of microfluidic chips in immunoassay. *Front. Bioeng. Biotechnol.* 10, 1112327.
- Yuste, I., et al., 2023. Engineering 3D-printed advanced healthcare materials for periprosthetic joint infections. *Antibiotics* 12 (8), 1229.
- Zang, L., et al., 2022. Not just anticoagulation—new and old applications of heparin. *Molecules* 27 (20), 6968.